Archaeal lipids trace ecology and evolution of marine ammonia-oxidizing archaea

Ronnakrit Rattanasriampaipong[a,1] , Yi Ge Zhang[a,1] , Ann Pearson[b] , Brian P. Hedlund[c], and Shuang Zhang[a]

Archaeal membrane lipids are widely used for paleotemperature reconstructions, yet these molecular fossils also bear rich information about ecology and evolution of marine ammonia-oxidizing archaea (AOA). Here we identified thermal and nonthermal behaviors of archaeal glycerol dialkyl glycerol tetraethers (GDGTs) by comparing the GDGT-based temperature index (TEX_{86}) to the ratio of GDGTs with two and three cyclopentane rings (GDGT-2/GDGT-3). Thermal-dependent biosynthesis should increase TEX_{86} and decrease GDGT-2/GDGT-3 when the ambient temperature increases. This presumed temperature-dependent (PTD) trend is observed in GDGTs derived from cultures of thermophilic and mesophilic AOA. The distribution of GDGTs in suspended particulate matter (SPM) and sediments collected from above the pycnocline—shallow water samples—also follows the PTD trend. These similar GDGT distributions between AOA cultures and shallow water environmental samples reflect shallow ecotypes of marine AOA. While there are currently no cultures of deep AOA clades, GDGTs derived from deep water SPM and marine sediment samples exhibit nonthermal behavior deviating from the PTD trend. The presence of deep AOA increases the GDGT-2/GDGT-3 ratio and distorts the temperature-controlled correlation between GDGT-2/GDGT-3 and TEX_{86}. We then used Gaussian mixture models to statistically characterize these diagnostic patterns of modern AOA ecology from paleo-GDGT records to infer the evolution of marine AOA from the Mid-Mesozoic to the present. Long-term GDGT-2/GDGT-3 trends suggest a suppression of today's deep water marine AOA during the Mesozoic–early Cenozoic greenhouse climates. Our analysis provides invaluable insights into the evolutionary timeline and the expansion of AOA niches associated with major oceanographic and climate changes.

tetraether lipids | ammonia-oxidizing archaea | marine archaeal ecology | archaea evolution

Nitrososphaerales (syn. *Thaumarchaeota*) form a deep-branching lineage within the phylum *Thermoproteota* (the amalgamation of the Thaumarchaeota-Aigarchaeota-Crenarchaeota-Korarchaeota (TACK) superphylum) (1). They are abundant in diverse settings, including terrestrial hot springs, soils, lacustrine environments, and marine sediments and waters—from epipelagic to hadopelagic zones (2–5). In modern oceans, cell counts suggest that *Nitrososphaerales* represents up to 20% of planktonic (2) and benthic (6) microbial communities. Moreover, they serve as chief autotrophic ammonia oxidizers in the water column (7, 8), making them critical players in marine nitrogen and carbon cycles.

It is widely believed that marine *Nitrososphaerales* evolved from thermophilic ammonia-oxidizing archaea (AOA) (9–14). Based on phylogenomic trees reconstructed from genomes of living archaea, marine AOA in the family *Nitrosopumilaceae* first evolved from terrestrial, thermophilic non-AOA before invading shallow marine settings, and more recently, they diversified and expanded into the deep ocean (14). However, the estimated ages of these steps remain controversial and not well understood. For example, two recent phylogenomics studies date the initial occurrence of marine AOA to two very different ages, 315 Ma (14) and 643 Ma (13). Additional independent evidence would allow us to constrain the evolutionary history of marine AOA better.

Isoprenoidal glycerol dialkyl glycerol tetraethers (GDGTs) are common membrane lipids found in both thermophilic and mesophilic *Nitrososphaerales* (15, 16). Core structures of GDGTs are ether-linked C_{40} biphytanes with a varying number of internal rings (abbreviated as GDGT-n, where n denotes the numbers of internal cyclopentane rings). Marine AOA belonging to the family *Nitrosopumilaceae* typically synthesize GDGTs with up to four cyclopentane rings (GDGT-0 to GDGT-4) as well as crenarchaeol (cren)—a unique GDGT containing four cyclopentane rings and one cyclohexane ring—and its isomer (cren′) (17) (Fig. 1). Crenarchaeol is likely a diagnostic biomarker of AOA (10, 21) as it is not observed outside of the AOA (22). Importantly, GDGTs are refractory to oxic degradation (23) and are preserved in immature marine sediments for at least the past 192 My (24).

Significance

Archaeal lipids are ubiquitous in marine sediments and are commonly used to infer past marine sea surface temperatures. However, these molecules can also be used to investigate the ecological and evolutionary history of marine archaea. Here we utilized data science techniques to identify two distinct patterns of archaeal lipid distribution from globally distributed seawater and surface sediments, indicative of shallow and deep ecotypes in the modern oceans. Further investigation of ancient marine sediments across the Mesozoic–Cenozoic suggests that deep water AOAs were suppressed in global oceans during greenhouse climates, which has not been observed by traditional molecular evolutionary models. This perspective carries important implications for marine nitrogen and carbon cycling and the reconstruction of past ocean temperatures.

Author affiliations: [a]Department of Oceanography, Texas A&M University, College Station, TX 77843; [b]Department of Earth and Planetary Sciences, Harvard University, Cambridge, MA 02138; and [c]School of Life Sciences, University of Nevada, Las Vegas, NV 89154

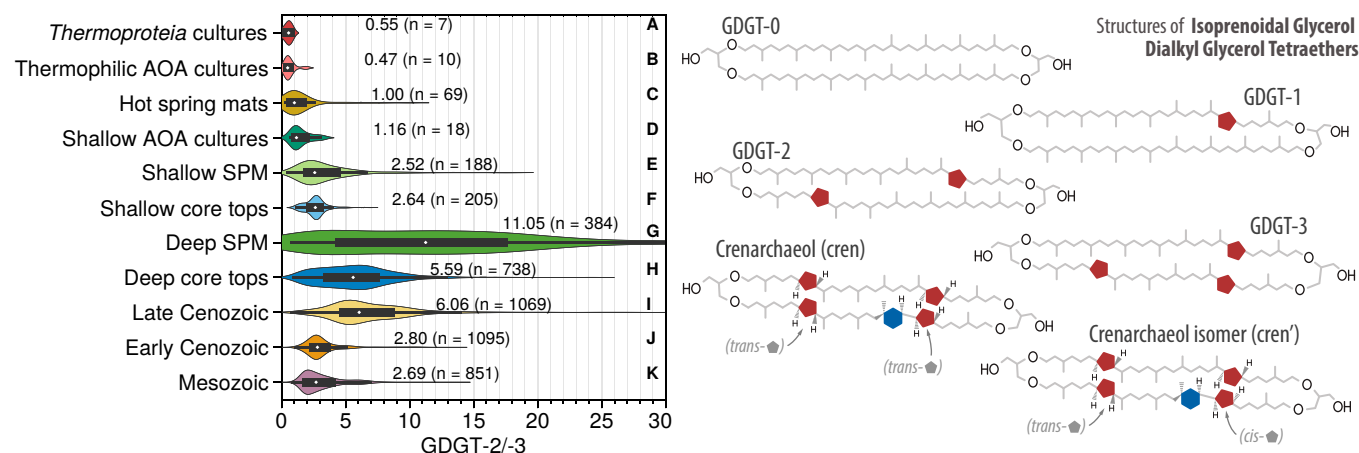[1]To whom correspondence may be addressed. Email: rrattan@tamu.edu or yige.zhang@tamu.edu.

Fig. 1. (*Left*) Ranges and distributions of GDGT-2/GDGT-3 ratios from different archives and (*Right*) structures of common GDGTs found in marine settings. (*A*) Cultures of thermophilic *Thermoproteia* (syn. *Crenarchaeota*). (*B*) Cultures of thermophilic AOA strains. (*C*) Environmental samples from terrestrial hot spring mats from sites with pH $\geqslant$ 6.5. (*D*) Cultures of known shallow AOA strains. Globally distributed SPM from (*E*) above (shallow SPM) and (*G*) below (deep SPM) the permanent pycnocline. Globally distributed surface (core top) sediments from sites sitting (*F*) above (shallow core tops) and (*H*) below (deep core tops) the permanent pycnocline. Open marine sediments from different geologic time intervals: (*I*) late Cenozoic (Oligocene–Holocene; 34 to 0 Ma), (*J*) early Cenozoic (Paleocene–Eocene; 66 to 34 Ma), and (*K*) Mesozoic (Early Jurassic–Cretaceous; 192 to 66 Ma). The median values (white dots), the interquartile range (black bars) of GDGT-2/GDGT-3 ratios, and the number of observations (n) associated with each group are also reported. Structures of six common GDGTs found in marine settings discussed throughout the main text are presented on the right. Stereochemistries of GDGTs shown here are based on revised structures following refs. 18–20.

The adjustment of internal structures of archaeal membrane lipids in response to thermal conditions—known as homeoviscous adaptation—is a common physiological response for both thermophilic (25–28) and mesophilic *Nitrososphaerales* (28–31). Although GDGT-0 and cren are always the predominant GDGTs in normal marine surface (core top) sediments, two main characteristics of samples from warm water regions are 1) higher GDGT-1, GDGT-2, GDGT-3, and cren′ compared to colder regions and 2) higher cren relative to GDGT-0 (29, 32). These empirical observations facilitated the development of TEX_{86} (TetraEther indeX of 86 carbon atoms) paleotemperature proxy (29):

$$TEX_{86} = \frac{[GDGT-2] + [GDGT-3] + [cren']}{[GDGT-1] + [GDGT-2] + [GDGT-3] + [cren']}.$$

Despite extensive use of TEX_{86} and other GDGT-based metrics to reconstruct ocean temperature history during the Mesozoic and Cenozoic (e.g., refs. 33–38), GDGT data are rarely used to study archaea themselves (cf. ref. 9), including their paleoecology or evolutionary history.

Here we demonstrate that the distribution of GDGTs from different archives, including pure cultures, marine settings, and terrestrial hot springs, can be linked to archaeal ecology and evolution. We first identified the thermal and nonthermal behaviors of GDGT pools based on the relationship between GDGT-2/GDGT-3 and TEX_{86} ratios. We then performed unsupervised clustering analyses to characterize these distinct patterns within ocean suspended particulate matter (SPM) that correspond to AOA communities separated by ocean density stratification. These diagnostic patterns of GDGTs then allow us to investigate the distribution and evolution of marine AOA since the Early Jurassic. Our work provides insight beyond typical paleotemperature reconstructions to understand the ecology and evolution of archaea in both modern and ancient oceans.

Results and Discussion

GDGT-2/GDGT-3 Differences Linked to Distinct Archaeal Communities. Ranges of GDGT-2/GDGT-3 are different between archaeal phylotypes and communities (Fig. 1). Low

GDGT-2/GDGT-3 ratios are observed in pure cultures of thermophilic *Thermoproteia* (syn. *Crenarchaeota*)—a sister group within the phylum *Thermoproteota* (1)—[median ($\bar{x}$) of 0.55; Fig. 1*A*] (39), pure cultures of thermophilic AOA ($\bar{x} = 0.47$; Fig. 1*B*) (40–42), and environmental samples collected from circum-neutral and alkaline photosynthetic hot spring mats ($\bar{x} = 1.00$; Fig. 1*C*) (27, 39, 43–48). Similarly, pure and enrichment cultures of the few cultivated marine AOA strains, all from the family *Nitrosopumilaceae*, synthesize GDGTs with relatively low GDGT-2/GDGT-3 ($\bar{x} = 1.16$; Fig. 1*D*) (28, 31, 41). To date, no pure or mixed cultures of deep water AOA are available for measurement.

The distribution of GDGTs in SPM throughout the water column suggests that the deep-dwelling archaeal communities have broader ranges of GDGT-2/GDGT-3 and higher average GDGT-2/GDGT-3 values than shallow communities (e.g., refs. 50, 51). Generally, GDGT-2/GDGT-3 ratios of SPM collected from above the permanent pycnocline—hereafter "shallow SPM"—are <5 ($\bar{x} = 2.52$; Fig. 1*E*). While slightly different from pure cultures of shallow water AOA ($\bar{x} = 1.16$; Fig. 1*D*), these relatively low GDGT-2/GDGT-3 values suggest that GDGTs derived from shallow SPM are predominantly sourced from AOA within the shallow planktonic community. Conversely, SPM collected from below the permanent pycnocline—hereafter "deep SPM"—has a much wider range of GDGT-2/GDGT-3 ($\bar{x} = 11.05$; Fig. 1*G*). The stark contrast across the pycnocline indicates that deep ocean AOA synthesize GDGTs differently from their shallow water relatives, consistent with earlier arguments that SPM collected from deep water is not dominated by sinking surficial material (50–52). The stratified distribution of GDGT-2/GDGT-3 is consistent with differences in the total archaeal lipidome observed in SPM from several oceanic regions (53) and fraction-specific hexose-phosphohexose intact polar lipids (IPLs)—a fraction derived from living and recently lysed cells—in the Eastern Tropical South Pacific (54).

Depth-related stratification of archaeal lipids in water columns agrees with studies of the distribution of AOA genes. Two distinct marine planktonic AOA clusters—water columns A and B—have been recognized in many samples based on PCR surveys of their ammonia monooxygenase (*amoA*) genes (55–58) and geranylgeranylglyceryl phosphate (GGGP) synthase (58). Water column A, related to *Candidatus* Nitrosopelagicus brevis

(NP-ϵ-2) (59, 60), represents the most abundant AOA in epipelagic and upper mesopelagic samples, whereas water column B (NP-α-2.2.2.1) (60), a separate species of *Candidatus Nitrosopelagicus* (1), is the most abundant AOA group in many mesopelagic and bathypelagic samples (55, 57).

Despite fewer effective export mechanisms of GDGTs in deep water (e.g., ref. 8), compound-specific studies of stable carbon and natural radiocarbon isotopic signatures indicate that GDGTs found in marine surface sediments are of mixed origin and may incorporate some deep water and/or sedimentary in situ production (50, 61, 62). Based on an extended dataset of core top sediments (63–66), GDGT-2/GDGT-3 ratios derived from sediments above the permanent pycnocline ($\bar{x}$ = 2.64; Fig. 1*F*)—hereafter "shallow core top sediments"—are similar to the signature of shallow SPM. In contrast, GDGTs collected from surface sediments below the permanent pycnocline—hereafter "deep core top sediments"—shift toward higher GDGT-2/GDGT-3 values and yield a value between deep and shallow SPM ($\bar{x}$ = 5.59; Fig. 1*H*). Although the export fraction of deep water GDGTs to global marine sediments remains unclear (e.g., ref. 67), the contribution of these lipids is high enough to partially overprint the low GDGT-2/GDGT-3 signatures that are carried by the dominant source of GDGTs sinking from shallow water, thereby affecting the final sedimentary GDGT composition.

Different patterns of GDGT-2/GDGT-3 ratios do not dramatically change TEX$_{86}$-SST estimates a priori since both compounds appear in the numerator and denominator of the TEX$_{86}$ ratio (29). However, strong deep water export of GDGTs to the sediments (as indicated by GDGT-2/GDGT-3 ratios) (52, 64) may influence regional proxy calibrations if these calibrations mix different proportions of samples derived from the three differently behaved environments: surface samples, deep SPM, and deep core tops. Statistical analyses of global core top TEX$_{86}$ vs. water temperatures at different depths show the best correlation for TEX$_{86}$ is surface to shallow subsurface waters (68, 69), while regional calibrations can yield different results [e.g., the Red Sea (70) and the Mediterranean Sea (64)]. Regardless, variations of GDGT-2/GDGT-3 distributions in marine core top sediments likely reflect different inputs.

Modern Distribution of GDGT-2/GDGT-3 Ratios Likely Reflects Community Differences. Raw data points and contour plots of the joint kernel density estimates (KDE) depict the shapes, patterns, and trends of each GDGT dataset (Fig. 2). Strong negative correlations between GDGT-2/GDGT-3 and TEX$_{86}$ ratios can be observed from cultured thermophilic archaea (*Thermoproteia* and AOA) and hot spring environmental samples (Fig. 2 *A*–*C*). This trend reflects the expected thermal-dependent biosynthesis of GDGTs. In culture studies, increased temperatures enhance the production of GDGTs with more ring structures (cf. refs. 26, 68, 69), which should increase TEX$_{86}$ but decrease GDGT-2/GDGT-3 ratios. The same relationship is observed for the few cultured strains of shallow water AOA (Fig. 2*D*). Thus, we established the presumed temperature-dependent (PTD) trend based on the orthogonal distance regression between GDGT-2/GDGT-3 and TEX$_{86}$ for GDGT data from all culture datasets combined (r^2 = 0.423, P = 3.543 × 10^{-5}) (dashed lines in all subplots of Fig. 2; *Materials and Methods* and *SI Appendix*, Fig. S1). We also calculated orthogonal distances between the established PTD trend and individual observations (OD$_{PTD}$) to reflect the relatedness between the distribution of GDGTs in each data type and the PTD trend (*SI Appendix*, Fig. S2). KDEs of OD$_{PTD}$ values from all types of cultures and hot spring mats (*SI Appendix*, Fig. S2 *A*–*D*) show

narrow, unimodal distributions with peaks centered near an OD$_{PTD}$ value of 0, reflecting that most data from these datasets are closely related to the PTD trend.

Shallow SPM and core top data (Fig. 2 *E* and *F*) as well as cultured shallow AOA (Fig. 2*D*) generally follow the established PTD trend, indicating that archaeal lipids produced by shallow water AOA exhibit thermal behavior. The observed thermal behavior from shallow core top sediments contrasts with the nonthermal behavior of the full dataset of modern core top sediments discussed by Taylor et al. (52). This nonthermal response is even more pronounced when only the deep water core top sediments are considered (Fig. 2*H*). In these data, GDGT-2/GDGT-3 increases with increasing TEX$_{86}$, in direct opposition to the presumed homeoviscous response. This pronounced nonthermal deviation from the PTD trend in deep water sediments highlights the apparent contribution of deep water SPM. The values of GDGT-2/GDGT-3 in deep water SPM show the broadest range of any subset of the data (Fig. 2*G*). Additionally, the KDEs of OD$_{PTD}$ values of deep SPM and sediments show widened, nonunimodal distributions with peaks at OD$_{PTD}$ > 0.5 (*SI Appendix*, Fig. S2 *G* and *H*), suggesting that most of these deep GDGT assemblages are unrelated to the PTD trend. We classify OD$_{PTD}$ = 0.5 to separate thermal and nonthermal data clusters (*SI Appendix*, Fig. S2) as it separates the two peaks observed in the deep core top dataset (*SI Appendix*, Fig. S2*H*). The different pattern in deep core top samples probably masks the thermal behavior of shallow core top samples when data are plotted together ("global core top") due to the high number of observations of deep core top samples.

Although deep water samples generally show a nonthermal pattern (Fig. 2 *G* and *H*), deep SPM samples from South China Sea (SCS) (73, 74) unexpectedly follow the PTD trend (red dots, Fig. 2*G*). Interestingly, this thermal pattern is not mirrored in deep core top sediments collected from the same region (75) (red dots, Fig. 2*H*). This inconsistency of GDGT distribution between deep SPM and deep core top sediment datasets might indicate a much higher export contribution of GDGTs synthesized by surface-dwelling AOA communities (cf. ref. 76), or it may reflect unusual exogenous sources to the SCS region (cf. ref. 77). For simplicity, we omitted the SCS samples in subsequent clustering analysis due to their unusual behavior.

Collectively, these PTD trends suggest that the shallow water masses (i.e., above pycnocline) are predominantly occupied by AOA communities with homogeneous, thermal GDGT responses to temperature, while the nonthermal pattern with a broad, nonunimodal KDE (*SI Appendix*, Fig. S2 *G* and *H*) likely reflects GDGT pools sourced from mixed AOA communities (i.e., shallow and deep). The thermal pattern potentially reflects GDGTs synthesized by natural archaeal communities as the pattern is well represented by studies of model organisms isolated from terrestrial hot springs (Fig. 2 *A*–*C*) or the shallow modern ocean (Fig. 2*D*).

Unsupervised Clustering Defines Shallow and Deep GDGT Assemblages. Because preclassification (i.e., shallow and deep) can be subject to label bias, we performed data clustering on the distribution of GDGT-2/GDGT-3 and TEX$_{86}$ using a Gaussian mixture model (GMM) algorithm (*Materials and Methods*), without offering the water depth information. This approach confirmed that the observed thermal and nonthermal patterns are indeed related to the distribution of archaeal ecotypes in the modern ocean. To best represent living archaeal communities, we also analyzed GDGTs derived from IPL fractions (53, 67, 78, 79), hereafter "SPM IPL-GDGTs," in addition to the original SPM dataset (Fig. 2 *E* and *G*) derived from both core lipid (CL) and total lipid (CL + IPL) fractions, hereafter "SPM total-GDGTs."
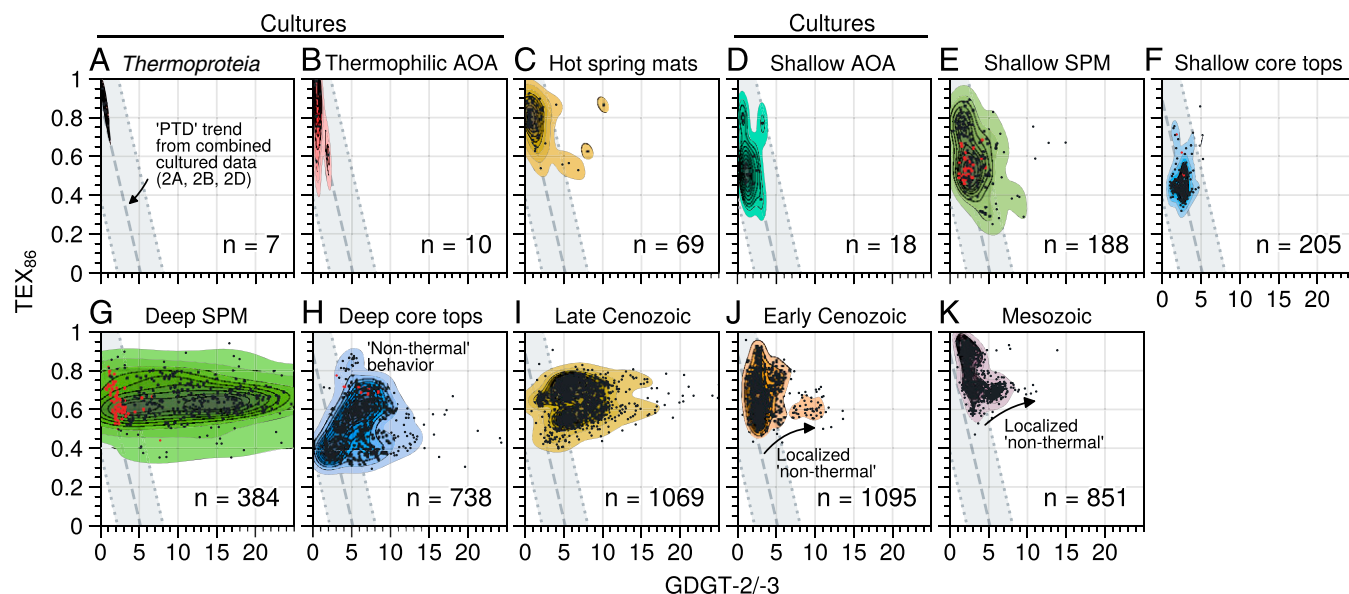
Fig. 2. Thermal and nonthermal behaviors of GDGTs from different archives. Scatterplots of GDGT-2/GDGT-3 ratios versus TEX$_{86}$. Panels with data from cultured samples are highlighted, while the rest of data are all from environmental samples. The order and colors of all subplots correspond to Fig. 1. GDGTs derived from (*A*) Cultures of thermophilic *Thermoproteia*, (*B*) pure cultures of thermophilic AOA, (*C*) hot spring mats, (*D*) cultures of shallow water AOA, (*E*) shallow SPM, and (*F*) shallow core top sediments follow the PTD trend. GDGTs from (*G*) deep SPM and (*H*) deep core top sediments show trends that deviate from the PTD trend. Samples from the (*K*) Mesozoic (Early Jurassic–Cretaceous; 192 to 66 Ma) and the (*J*) early Cenozoic (Paleocene–Eocene; 66 to 34 Ma) also largely follow the PTD trend, while the (*I*) late Cenozoic (Oligocene–Holocene; 34 to 0 Ma) pattern resembles modern deep sediments and SPM. Red dots in *E–H* are data from the SCS. Contour plots of joint KDE (shaded, colored regions) are plotted with a contour interval of 0.1 from the joint density of 0.1 (outer rim) to 0.9 (core). Dashed gray lines in all subplots show the established PTD trend. Shaded gray areas represent ranges of OD$_{PTD}$ that approximately follow thermal ($0 \leqslant OD_{PTD} \leqslant 0.5$) behaviors.

GMM treats data as a mixture of probability distributions (i.e., K components) and finds clusters by maximizing the probability that each data point belongs to each specific cluster. Here K represents an inferred number of archaeal clusters in marine environments, for which the expected value is 2. However, for thoroughness, we first generated different estimates of K using two criteria: Bayesian information criterion (BIC) and average silhouette scores (SS); optimization is achieved at low BIC and high SS. We used hard clustering for data points positioned in a region where two or more Gaussian components overlap; i.e., these occurrences are assigned to the Kth component having the higher probability of such instances.

For both the SPM total-GDGT dataset and the SPM IPL-GDGT dataset, $K = 2$ provides the highest SS, while $K = 3$ gives the lowest BIC (Fig. 3 *A* and *B*). Values of $K > 3$ yield notably poorer quality of clusters (particularly SS values) for both datasets. Because of the marked decrease in SS for SPM IPL-GDGT at $K = 3$ (Fig. 3*B*), we view $K = 2$ as the overall best estimate for the number of GMM components across all the data. Silhouette plots—clusters 0 (C0, blue) and 1 (C1, orange)—show the relatedness of individual data points to their assigned clusters (Fig. 3*C*). High positive values mean such data points likely belong to the assigned cluster, while negative values reflect poor relatedness of the data to their assigned clusters.

Clusters C0 and C1 (Fig. 3*D*) resemble the nonthermal and thermal patterns of preclassified deep and shallow SPM datasets (Fig. 2 *E* and *G*), respectively, despite being created agnostic of any depth information. The GMM results show a more distinct separation between the two clusters compared to the overlapping envelopes of deep (dotted line) and shallow (dashed line) groupings (Fig. 3*D*). On the pressure-temperature-salinity (p-t-s) diagram, the SPM samples assigned to each GMM cluster mostly occupy different water masses in the ocean (Fig. 3*E*), with few cases where GDGT patterns cross the pycnocline. The approximate boundary between C0 and C1 is $\sigma_T \approx 26.5$

(or $\sigma_T \approx 28.5$ in the Mediterranean). At the 95% significance threshold, pairwise comparisons of the two-sample Kolmogorov–Smirnov test confirm that 1) GDGT distributions of labeled vs. label-free clusters (i.e., shallow SPM vs. C1 and deep SPM vs. C0) are not statistically different and 2) the distributions of clusters with different thermal patterns (i.e., C1 vs. C0 and shallow SPM vs. deep SPM) are statistically different (*Materials and Methods* and *SI Appendix*, Fig. S4). We also calculated results for $K = 3$ for the SPM total-GDGT dataset, which also clearly captured the thermal behaviors (*SI Appendix*, Fig. S5). Data with nonthermal behavior were split into two smaller clusters with poorer SS (*SI Appendix*, Fig. S5).

The fact that GMM clustering recognizes the thermal distribution pattern in SPM without prior knowledge of water depth or position relative to the pycnocline supports the idea of a distinct GDGT profile of the shallow archaeal community in the modern ocean. Poor clustering results of the nonthermal pattern ($K = 2$ or 3 for deeper samples) emphasize that GDGTs from deep water masses represent mixed sources. Importantly, our results support the idea that when archaeal ecotypes are distinguished by different GDGT distributions, these community signals can be disentangled in complex datasets.

Inferring Ecological Changes of Marine AOA in Past Oceans. Expanding on existing GDGT compilations from the Cretaceous (37) and the Eocene (36), we examined GDGT-2/GDGT-3 changes over the past 192 My from a composite marine record of GDGT data—containing over 3,000 entries spanning from the Early Jurassic to the Holocene (*Materials and Methods*). Samples with excessive soil input (measured by the BIT index) (80), methanogenic archaea inputs (measured by the %GDGT-0) (81, 82), and methanotrophic archaea (measured by methane index) (83) were screened out of this database (*SI Appendix*). The median GDGT-2/GDGT-3 values progressively increased from an exclusively low, shallow-like GDGT-2/GDGT-3 signature
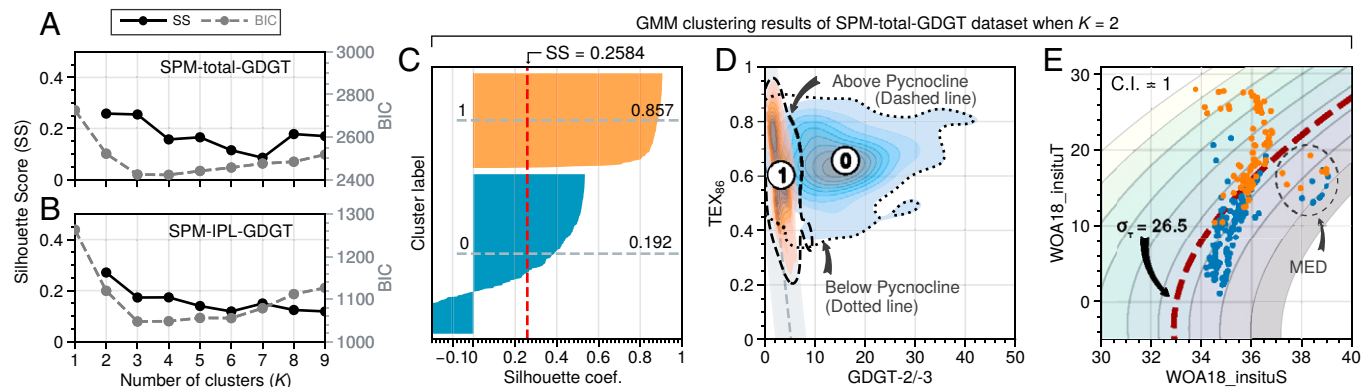
Fig. 3. Clustering analysis of modern SPM based on GMM clustering algorithm. The consensus number of clusters (*K*) is 2. Average SS based on MD and BIC from *K* = 1 to *K* = 9 for (*A*) SPM-total-GDGT and (*B*) SPM-IPL-GDGT. (*C*) Silhouette plots of the two resulting clusters. Horizontal gray lines show the average SS of each cluster. A vertical red line shows the average SS for the entire dataset. (*D*) Contour plots of joint KDE for cluster 0 (C0; blue) and cluster 1 (C1; orange) with a contour interval of 0.1, from KDE = 0.1 to 0.9. The distribution pattern of the two clusters resembles the shallow and deep groups as shown in Fig. 2 *E* and *G*. (*E*) Density contours (σ_T on p-t-s diagram) suggest C1 and C0 reflect shallow (less dense) and deep (denser) water masses, respectively. MED, Mediterranean Sea.

during the Mesozoic ($\bar{x}$ = 2.69, 192 to 66 Ma; Fig. 1*K*) and early Cenozoic ($\bar{x}$ = 2.80, 66 to 34 Ma; Fig. 1*J*) to the deep core top GDGT-2/GDGT-3 signature during the middle to late Cenozoic ($\bar{x}$ = 6.07, 34 to 0 Ma; Fig. 1*I*). Although many notable GDGT records from the Mesozoic and early Cenozoic come from shallow (shelf) sites, we find these low GDGT-2/GDGT-3 signatures and thermal GDGT distribution patterns (*SI Appendix,* Fig. S6) cannot be explained by preferential sampling of shallow sites. Paleo–water depth estimates of the Mesozoic and early Cenozoic datasets based on the paleo–digital elevation models (PaleoDEMS) (84) include deep water locations (*Materials and Methods* and *SI Appendix,* Table S3). Preferential degradation also seems unlikely since diagenesis experiments do not show evidence of preferential degradation of GDGT-3 over GDGT-2 (85). Thus, these shifts with time represent true variations related to the depositional sources of GDGTs.

The relationship between GDGT-2/GDGT-3 and TEX$_{86}$ has also changed over geological history (Fig. 2 *I–K*). Most GDGTs during the Mesozoic and early Cenozoic exhibit the thermal behavior (Fig. 2 *J* and *K*) with a tight, unimodal PTD trend (OD$_{PTD}$ < 0.5; *SI Appendix,* Fig. S2 *J* and *K*). This suggests that GDGT pools in pre-Oligocene oceans were predominantly derived from archaeal communities having a single AOA ecotype. Due to the similar patterns observed in Mesozoic, early Cenozoic, and modern SST-controlled shallow SPM and core top sediments (Fig. 2 *E* and *F*), we suggest that ancient archaeal communities resembled today's shallow AOA ecotypes and lived in, or communicated with, the epipelagic zone. Alternatively, the epipelagic zone could have had minimal AOA population due to constraints such as low ammonia availability as a consequence of inefficient biological pump. In contrast, the thermal behavior of GDGT-2/GDGT-3 is largely absent in sediments from the late Cenozoic (Fig. 2*I*). These late Cenozoic GDGTs mimic modern deep water SPM and core top sediments (Fig. 2 *G* and *H*) in having a broad, nonunimodal PTD trend (OD$_{PTD}$ ⩾ 0.5; *SI Appendix,* Fig. S2*I*). We interpret GDGTs with unusually high GDGT-2/GDGT-3 ratios as a diagnostic fingerprint of today's deep AOA communities and consequently lead to nonthermal distribution patterns of GDGT-2/GDGT-3 signals. This view is consistent with arguments that Eocene and Cretaceous GDGT distributions generally are not analogous to modern GDGT assemblages (38). Interestingly, some Mesozoic and early Cenozoic marine sediments do record the nonthermal pattern (arrows in Fig. 2 *J* and *K*), suggesting that

AOA communities with the deep water AOA GDGT fingerprint have locally occupied Mesozoic and early Cenozoic deep oceans before radiating into the global ocean in the late Cenozoic. The temporal shift in these patterns could mark structural changes in AOA communities in past deep oceans or a global expansion of deep water AOA niches.

Linking Archaeal Ecology and Evolution to Oceanographic and Climate Change. We repeated the GMM clustering for the expanded marine Mesozoic–Cenozoic GDGT database, again with *K* = 2. Cluster C1 (orange) exhibits a thermal pattern that strongly follows the established PTD trend, while cluster C0 (blue) shows the nonthermal pattern (Fig. 4*A*). More interestingly, the covariance between GDGT-2/GDGT-3 and TEX$_{86}$ of C1 appears to follow OD$_{PTD}$ ⩽ 0.5 (shaded gray area, Fig. 4*A*), suggesting that the relationship between GDGT-2/GDGT-3 and TEX$_{86}$ within C1 behaves in agreement with the modern PTD trend.

The spatiotemporal distribution of paleolipids suggests that archaeal communities in past oceans may be linked to major oceanographic and climatic transitions. The distribution patterns of C0 and C1 on GDGT-2/GDGT-3-vs.-TEX$_{86}$ scatterplots have gradually shifted from predominantly thermal (Mesozoic to early Cenozoic) to largely nonthermal behaviors (late Cenozoic) (Figs. 4 *B–D*). A GDGT-2/GDGT-3 cutoff value of 5 separates C1 from C0 across the entire studied interval, while the medians of age-binned data generally fluctuate (especially for C0) (Fig. 4*E*). Based on normalized density estimates between C0 and C1 over the past 192 My, shallow AOA communities dominated marine settings from the middle Cretaceous (ca. 110 Ma) up until the Eocene–Oligocene transition (EOT) (Fig. 4*F*). Oceanic crustal subsidence is expected to gradually increase water depth of study sites with time, with the strongest influence on the older, Mesozoic–early Cenozoic samples (cf. ref. 86). However, paleo–water depth estimates of these shallow-like C1 clusters range from 0 to >2,000 mbsl (Fig. 4*G*), confirming that the observed patterns are not biased by only sampling shallow water environments. Subsampling analyses without shallow water samples, including 1) clustering analyses of samples only associated with deep water (>100 mbsl) (*SI Appendix,* Fig. S7) and 2) visual inspections of ancient GDGTs with estimated paleodepth above and below 100 mbsl (*SI Appendix,* Fig. S6), as well as altering the cutoff between shallow and deep to 1,000 m for analyses 1 and 2, all do not change this conclusion.
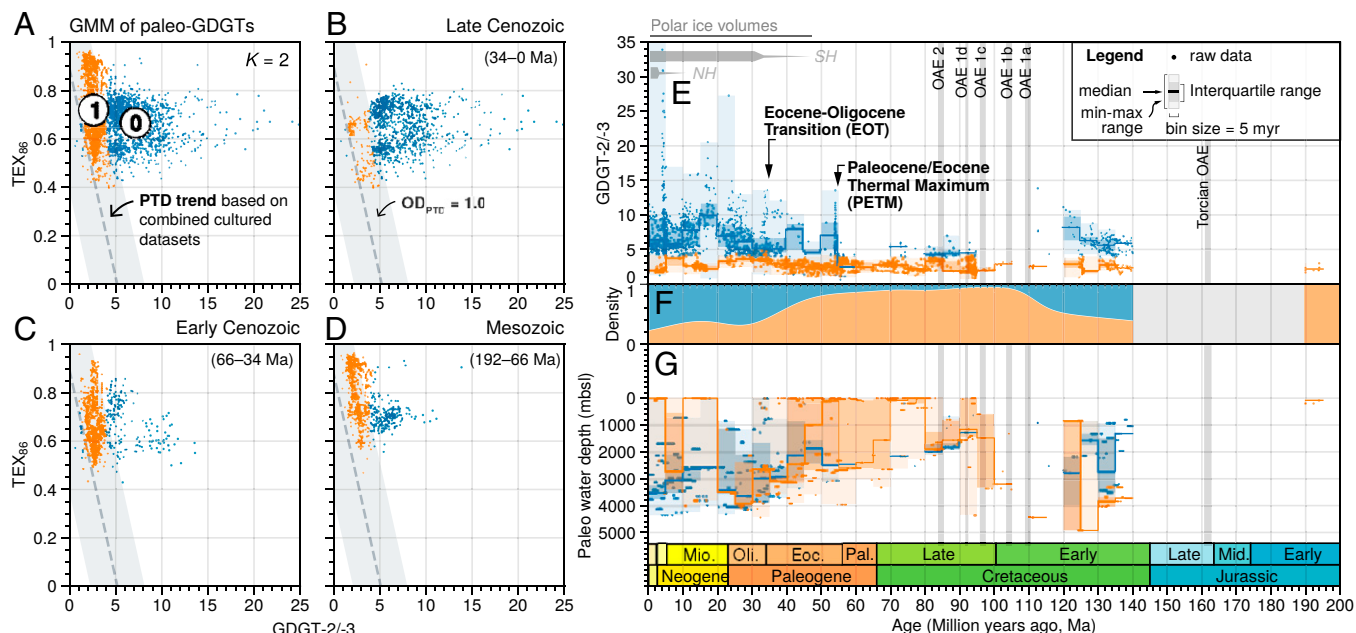
Fig. 4. The evolution of GDGT clusters over the past 192 My. (*A*) Two GMM clusters for the entire ancient GDGT dataset. Cluster 1 (orange) exhibits the thermal pattern, while cluster 0 (blue) shows the nonthermal pattern deviating from the established PTD trend (dashed line). Scatterplots of resulting clusters during each geologic time interval: (*B*) late Cenozoic (Oligocene–Holocene; 34 to 0 Ma), (*C*) early Cenozoic (Paleocene–Eocene; 66 to 34 Ma), and (*D*) Mesozoic (Early Jurassic–Cretaceous; 192 to 66 Ma). (*E*) Evolution of GDGT-2/GDGT-3 over geologic time for C0 and C1 with 5-My binned values including medians (middle lines), interquartile range (darker shaded boxes), and minimum-maximum range (lighter shaded boxes). (*F*) Proportion of data density between C0 and C1 based on kernel density estimates. (*G*) Paleo–water depth estimates based on paleogeographic maps from the PaleoDEMS project. Labeled major climatic and oceanic anoxic events with relative ice volumes are modified from refs. 87 and 88.

Intriguingly, the dominance of the shallow AOA C1 cluster occurred during the Late Cretaceous–early Paleogene, a predominantly warm greenhouse climate interval (e.g., refs. 37, 87, 89). In contrast, the occurrence of the deep AOA C0 cluster in marine settings increases during colder intervals, including some evidence that C0 existed during the relatively cooler Early Cretaceous (37) and the Cenozoic icehouse periods (late Paleogene–Holocene) (e.g., refs. 87, 88, 90). This suggests that community structures of marine AOA are linked to Earth's past climates. Niche expansion and segregation of distinct AOA groups are potentially related to changes in ocean circulation, thermal stratification, and carbon/nutrient cycling. For example, the shift from C1- to C0-dominated oceans during the lead-up to the EOT coincided with dramatic changes in the mode of meridional overturning circulation at about 34 Ma (91). Climate modeling and benthic $\delta^{18}O$ records have suggested that Antarctic glaciation at 34 Ma caused major ocean restructuring, with enhanced production and transport of Antarctic bottom water and Antarctic intermediate water and increased stratification (92, 93). In addition to changes in ocean circulation, a strengthened biological pump due to cooler temperatures (94, 95) may have increased export productivity and ammonium regeneration, resulting in favorable conditions for AOA in the deep sea. It is important to note that the dominance of each GMM cluster over time is based on available ancient GDGT information. These observed Mesozoic trends might be subject to geographical biases due to low data density and fewer represented sites (*SI Appendix*, Fig. S8).

Current phylogenetic timelines for the evolution of type B deep AOA predate the availability of GDGTs in rock records [~309 Ma according to Yang et al. (14); or ~643 Ma according to Ren et al. (13)]. Consequently, the current GDGT database cannot directly test these ages. Nevertheless, GDGT data presented here suggest that deep AOA clades evolved before 140 Ma, which is consistent with the phylogenomic work. More importantly, since phylogenic

trees do not reflect the abundance of past or present AOA, GDGT data allow us to evaluate the spatiotemporal changes of AOA that are sufficiently abundant to affect the GDGT composition of the sedimentary record, yielding insights into AOA evolution and ecology. Our perspective suggests that deep AOA communities may have invaded the deep oceans by the early Mesozoic but were largely suppressed during the Late Cretaceous to Paleogene greenhouse. Future investigation is needed to examine the responses of marine archaeal communities to environmental forcings. In either case, the perspectives from this work improve our understanding of the evolutionary and ecological history of marine AOA.

Conclusion

Intrinsic distributions of archaeal lipid assemblages have rarely been used to study the ecology and evolution of archaea in past oceans. Building upon Taylor et al. (52) and the whole-assemblage machine learning approach of Dunkley Jones et al. (38), we used GDGT-2/GDGT-3 ratios to infer changes in marine archaeal ecology over the geologic past. The clear distinction of GDGT-2/GDGT-3 signatures between shallow and deep marine samples support taxonomic arguments for two distinct groups of AOA in the ocean water column (e.g., refs. 53, 58). These same patterns are observed to segregate temporally in marine sediments, suggesting there were ecological shifts of archaeal communities in past oceans. The abrupt shift in GDGT-2/GDGT-3 values and distribution patterns of GDGTs during the EOT suggests niche expansion of deep archaeal clades and implies that changes in archaeal ecology in past oceans were associated with major shifts in Earth's climatic and oceanographic state. These insights carry important implications for marine nitrogen and carbon cycling and the reconstruction of past ocean temperatures. Although the nonuniform spatiotemporal distribution of paleodatasets may not be globally representative and might influence the GMM

clustering results, our study provides a framework for future investigation that can be easily performed using community-built statistical tools when more data are available.

Materials and Methods

Data Compilation and Prescreening. Original raw or fractional GDGT abundances ($n = 4,798$) of seven different archives are compiled from 79 publications (SI Appendix, Fig. S9). Our collection is an expansion of previous GDGT compilations, including globally distributed core top sediments for SST-TEX$_{86}$ calibrations (64, 65) as well as ancient marine sediments deposited during the Eocene (36) and Cretaceous (37) periods. We removed any GDGT measurements with very low reported abundances ($\leqslant 0.001$ out of 1 or $\leqslant 0.1\%$) of each GDGT fraction to avoid some potential below detection limit values (SI Appendix, Fig. S10) except for GDGT measurements derived from thermophilic Archaea (SI Appendix). We primarily used numeric ages as reported in the literature. When needed, we updated age models relative to the Geologic Time Scale 2012 (GTS2012) (96) based on available biostratigraphic zones (biozones). Age differences between GTS2012 and the more recent GTS2020 (97) do not substantially change the overall temporal distribution of GDGT data in this study (SI Appendix, Fig. S11). A full list of data sources can be found in SI Appendix, Table S1 for modern archives and SI Appendix, Table S2 for paleoarchives. Screening criteria for our composite GDGT database are described in detail in SI Appendix.

Linear Regressions for the PTD Trend Determination. With a limited number of data points from culture data, we determined the PTD trend based on combined data from three different sets, including 1) *Thermoproteia* cultures, 2) thermophilic AOA cultures, and 3) shallow water AOA cultures (SI Appendix, Fig. S1A). We performed three different linear regression techniques: 1) orthogonal distance regression (ODR), 2) direct ordinary least square (OLS), and 3) reverse OLS. As GDGT-2/GDGT-3 and TEX$_{86}$ are two independent variables, we established the PTD trend based on the ODR of the combined dataset to avoid regression dilutions (i.e., different regression slopes as OLS techniques assume one of the variables to be error-free). Additionally, the ODR provides improved correlation coefficients across all testing scenarios (SI Appendix, Fig. S1B). The regressions were performed in the Python programming language (98). For OSL regressions, we used *sklearn.linear_model.LinearRegression* from the community-built machine learning library Scikit-learn (99). For ODR regressions, we used *scipy.ODR* module from the SciPy library (100).

Ocean Layer Determination for Modern SPM and Core Top Sediments. Seawater density calculations, statistical analysis, and seawater density (sigma-T or σ_T) were performed in Python using the Xarray package (101). We used objectively analyzed monthly climatological means of seawater temperature (t_an) (102) and salinity (s_an) (103) on the $0.25° \times 0.25°$ grid for all available decades (1955 to 2017) from the World Ocean Atlas 2018 (WOA18) to calculate monthly climatological means of σ_T following Millero and Poisson's (104) 1-atm equation of state of seawater. Then, we calculated SD of the constructed σ_T with respect to time to evaluate seasonal variations of seawater density for global oceans. Next, we mapped calculated σ_T values from the nearest grid cells to modern SPM and core top sediments based on associated geographical coordinates and water depth of individual GDGT measurements. Cross-sections of ocean basins show that permanent pycnoclines (≈ 100 mbsl) and deeper water masses are associated with $SD_{sigma-T} < 0.1$ (SI Appendix, Fig. S12). Thus, we used a contour line of $SD_{sigma-T} = 0.1$ as a depth of determination for shallow ($SD_{sigma-T} \geqslant 0.1$) and deep ($SD_{sigma-T} < 0.1$) GDGT samples.

In Situ Temperatures and Salinities for Water Column SPM. To display water column SPM data on the p-t-s diagram, seawater temperature (t_an) (102) and salinity (s_an) (103) from the WOA18 objectively analyzed annual climatological means on the $0.25° \times 0.25°$ grid for all available decades (1955 to 2017) were used to assign in situ seawater temperatures (WOA18_insituT) and salinities (WOA18_insituS) to individual GDGT measurements derived from water column SPM.

Paleogeographical Location Reconstructions and Paleo–Water Depth Estimation of Ancient Marine Sediments. We used *pyGplates*–a Python-based scripting interface to the plate tectonics open-source software GPlates

(105)–to reconstruct geographical locations of ancient marine sediments at the time of deposition. We used rotation (ROT) and static polygon (GMPL) files that were used in the PaleoDEMS project (84) to reconstruct paleolocations of all paleo-GDGT measurements. Then, we mapped the reconstructed paleolatitudes and paleolongitudes to the nearest grid cells from the $1° \times 1°$ PaleoDEMS gridded paleobathymetry to extract associated paleo–water depth estimates. We readjusted any paleo–water depth estimates that are above sea level, apparently due to the uncertainty of the PaleoDEMS data, to be 0 mbsl or at sea level. SI Appendix, Table S3 summarizes our expanded compilation of paleo–water depth information with associated published estimates from independent studies.

We compared median values of the resulting depths with the published values to evaluate the quality of paleo–water depth estimates in our study. Paleo–water depths based on the PaleoDEMS dataset largely agree with available published data (SI Appendix, Fig. S13, filled symbols). On some occasions, the PaleoDEMS estimates are much deeper than the published values (SI Appendix, Fig. S13, open symbols). These mismatches can be due to the difference of paleo–water depth reconstruction methods: 1) reported paleodepths from initial drilling reports are often based on sedimentological and micropaleontological evidence at local sites, whereas 2) PaleoDEMS paleobathymetry is based on thermal subsidence models. In an area with a complex paleobathymetry (e.g., shallow seamounts), the PaleoDEMS data may give deeper paleo–water depth estimates than the local evidence as a much deeper abyssal plain can bias the estimates. For example, the PaleoDEMS estimates of the Arctic Coring Expedition site during the EOT are much deeper than those reported by independent studies (SI Appendix, Table S3) as the PaleoDEMS may not accurately reconstruct the paleo–water depths of the Lomonosov Ridge. However, the presence of reworked shallow water sediments in deep sea settings can sometimes bias the estimates derived from locally observed sedimentology/micropaleontology [e.g., turbidite sediments at Site 1172 during the late Eocene (38 to 34 Ma) (106)]. Paleogeographical reconstructions with higher spatiotemporal resolutions may provide closer paleo–water depth estimates compared to the reported values. Future local and/or regional studies need to confirm the interpreted paleosettings on a case-by-case basis.

GMM Clustering Analysis. We used the *GaussianMixture* function from the *sklearn.mixture* module to extract a mixture of probability distributions from two input variables: GDGT-2/GDGT-3 and TEX$_{86}$. We performed clustering analysis with different predetermined numbers of K components ranging from 1 to 9. Each clustering scenario was evaluated based on visualizations and two quality control matrices, including BIC from the *GaussianMixture* function and average SS from the *sklearn.metrics* module. Unlike the K-Means clustering algorithm that partitions data points based on only cluster means, the GMM clustering technique takes the covariances (i.e., shape of the joint distribution) of the clusters into consideration (107), which seems to be a more appropriate algorithm given the noncircular distributions on the joint KDE plots. As the expected patterns are likely nonspherical, we used Mahalanobis distance (MD) as a distance metric for the SS calculation instead of the Euclidean distance (cf. ref. 108). In the case of similar BIC and SS from multiple K scenarios, the lower K scenario is preferred.

Two-Sample Kolmogorov–Smirnov Test for Goodness of Fit. To investigate the significance of the difference between cumulative distribution functions (CDFs) of water column SPM, we perform the nonparametric test two-sample Kolmogorov–Smirnov (KS) using the *ks_2samp* function from the *scipy.stats* module (100) for GDGT-2/GDGT-3 and TEX$_{86}$ attributes. The two-sample KS test measures vertical distances between CDFs of two input datasets and returns the maximum distance (D_{max}) as the KS statistic as well as associated P values. The resulting D_{max} is then compared to the vertical distance at the 5% critical value (critical $D_{0.05}$). If $D_{max} >$ critical $D_{0.05}$ or $P < 0.05$, we reject the null hypothesis that the two sample distributions are identical, and vice versa. Pairwise comparisons of KS statistics and CDFs of SPM total-GDGTs and IPL-GDGTs are shown in SI Appendix, Fig. S4.

Data Availability. Preprocessing and postprocessing datasets (XLSX) (108) as well as Jupyter Notebooks (IPYNB) containing Python codes (109) that were used for data preparation, statistical and unsupervised clustering analyses, and data visualization are deposited at cited Figshare repositories (108, 109) and available

1. C. Rinke *et al.*, A standardized archaeal taxonomy for the Genome Taxonomy Database. *Nat. Microbiol.* **6**, 946–959 (2021).
2. M. B. Karner, E. F. DeLong, D. M. Karl, Archaeal dominance in the mesopelagic zone of the Pacific Ocean. *Nature* **409**, 507–510 (2001).
3. G. J. Herndl *et al.*, Contribution of Archaea to total prokaryotic production in the deep Atlantic Ocean. *Appl. Environ. Microbiol.* **71**, 2303–2309 (2005).
4. H. Agogué, M. Brink, J. Dinasquet, G. J. Herndl, Major gradients in putatively nitrifying and non-nitrifying Archaea in the deep North Atlantic. *Nature* **456**, 788–791 (2008).
5. A. E. Santoro, R. A. Richter, C. L. Dupont, Planktonic marine Archaea. *Annu. Rev. Mar. Sci.* **11**, 131–158 (2019).
6. T. Hoshino, F. Inagaki, Abundance and distribution of Archaea in the subseafloor sedimentary biosphere. *ISME J.* **13**, 227–231 (2019).
7. M. Könneke *et al.*, Isolation of an autotrophic ammonia-oxidizing marine archaeon. *Nature* **437**, 543–546 (2005).
8. C. Wuchter *et al.*, Archaeal nitrification in the ocean. *Proc. Natl. Acad. Sci. U.S.A.* **103**, 12317–12322 (2006).
9. M. M. M. Kuypers *et al.*, Massive expansion of marine archaea during a mid-Cretaceous oceanic anoxic event. *Science* **293**, 92–95 (2001).
10. J. S. Damsté, S. Schouten, E. C. Hopmans, A. C. van Duin, J. A. Geenevasen, Crenarchaeol: The characteristic core glycerol dibiphytanyl glycerol tetraether membrane lipid of cosmopolitan pelagic crenarchaeota. *J. Lipid Res.* **43**, 1641–1651 (2002).
11. M. Groussin, M. Gouy, Adaptation to environmental temperature is a major determinant of molecular evolutionary rates in archaea. *Mol. Biol. Evol.* **28**, 2661–2674 (2011).
12. Z. S. Hua *et al.*, Genomic inference of the metabolism and evolution of the archaeal phylum Aigarchaeota. *Nat. Commun.* **9**, 2832 (2018).
13. M. Ren *et al.*, Phylogenomics suggests oxygen availability as a driving force in Thaumarchaeota evolution. *ISME J.* **13**, 2150–2161 (2019).
14. Y. Yang *et al.*, The evolution pathway of ammonia-oxidizing Archaea shaped by major geological events. *Mol. Biol. Evol.* **38**, 3637–3648 (2021).
15. M. De Rosa, A. Gambacorta, The lipids of archaebacteria. *Prog. Lipid Res.* **27**, 153–175 (1988).
16. S. Schouten, E. C. Hopmans, R. D. Pancost, J. S. Damste, Widespread occurrence of structurally diverse tetraether membrane lipids: Evidence for the ubiquitous presence of low-temperature relatives of hyperthermophiles. *Proc. Natl. Acad. Sci. U.S.A.* **97**, 14421–14426 (2000).
17. G. N. Inglis, J. E. Tierney, *The TEX86 Paleotemperature Proxy* (Elements in Geochemical Tracers in Earth System Science, Cambridge University Press, 2020).
18. X. L. Liu, J. S. Lipp, D. Birgel, R. E. Summons, K. U. Hinrichs, Predominance of parallel glycerol arrangement in archaeal tetraethers from marine sediments: Structural features revealed from degradation products. *Org. Geochem.* **115**, 12–23 (2018).
19. J. S. Sinninghe Damsté *et al.*, The enigmatic structure of the crenarchaeol isomer. *Org. Geochem.* **124**, 22–28 (2018).
20. M. Holzheimer *et al.*, Total synthesis of the alleged structure of crenarchaeol enables structure revision. *Angew. Chem. Int. Ed. Engl.* **60**, 17504–17513 (2021).
21. J. R. de la Torre, C. B. Walker, A. E. Ingalls, M. Könneke, D. A. Stahl, Cultivation of a thermophilic ammonia oxidizing archaeon synthesizing crenarchaeol. *Environ. Microbiol.* **10**, 810–818 (2008).
22. A. Pearson, A. E. Ingalls, Assessing the use of archaeal lipids as marine environmental proxies. *Annu. Rev. Earth Planet. Sci.* **41**, 359–384 (2013).
23. S. Schouten, E. C. Hopmans, J. S. Sinninghe Damsté, The effect of maturity and depositional redox conditions on archaeal tetraether lipid palaeothermometry. *Org. Geochem.* **35**, 567–571 (2004).
24. S. A. Robinson *et al.*, Early Jurassic North Atlantic sea-surface temperatures from TEX$_{86}$ palaeothermometry. *Sedimentology* **64**, 215–230 (2017).
25. M. De Rosa, E. Esposito, A. Gambacorta, B. Nicolaus, J. D. Bu'Lock, Effects of temperature on ether lipid composition of *Caldariella acidophila*. *Phytochemistry* **19**, 827–831 (1980).
26. A. Gliozzi, G. Paoli, M. De Rosa, A. Gambacorta, Effect of isoprenoid cyclization on the transition temperature of lipids in thermophilic archaebacteria. *Biochim. Biophys. Acta Biomembr.* **735**, 234–242 (1983).
27. J. J. Paraiso *et al.*, The distribution and abundance of archaeal tetraether lipids in U.S. Great Basin hot springs. *Front. Microbiol.* **4**, 247 (2013).
28. W. Qin *et al.*, Confounding effects of oxygen and temperature on the TEX86 signature of marine Thaumarchaeota. *Proc. Natl. Acad. Sci. U.S.A.* **112**, 10979–10984 (2015).
29. S. Schouten, E. C. Hopmans, E. Schefuss, J. S. Sinninghe Damsté, Distributional variations in marine crenarchaeotal membrane lipids: A new tool for reconstructing ancient sea water temperatures? *Earth Planet. Sci. Lett.* **204**, 265–274 (2002).
30. C. Wuchter, S. Schouten, S. G. Wakeham, J. S. Sinninghe Damsté, Temporal and spatial variation in tetraether membrane lipids of marine Crenarchaeota in particulate organic matter: Implications for TEX$_{86}$ paleothermometry. *Paleoceanography* **20**, PA3013 (2005).
31. F. J. Elling, M. Könneke, M. Mußmann, A. Greve, K. U. Hinrichs, Influence of temperature, pH, and salinity on membrane lipid composition and TEX$_{86}$ of marine planktonic thaumarchaeal isolates. *Geochim. Cosmochim. Acta* **171**, 238–255 (2015).
32. Y. G. Zhang, M. Pagani, Z. Wang, Ring index: A new strategy to evaluate the integrity of TEX$_{86}$ paleothermometry. *Paleoceanography* **31**, 220–232 (2016).
33. P. K. Bijl *et al.*, Early Palaeogene temperature evolution of the southwest Pacific Ocean. *Nature* **461**, 776–779 (2009).
34. Z. Liu *et al.*, Global cooling during the Eocene-Oligocene climate transition. *Science* **323**, 1187–1190 (2009).
35. Y. G. Zhang, M. Pagani, Z. Liu, A 12-million-year temperature history of the tropical Pacific Ocean. *Science* **344**, 84–87 (2014).
36. G. N. Inglis *et al.*, Descent toward the icehouse: Eocene sea surface cooling inferred from GDGT distributions. *Paleoceanography* **30**, 1000–1020 (2015).
37. C. L. O'Brien *et al.*, Cretaceous sea-surface temperature evolution: Constraints from TEX$_{86}$ and planktonic foraminiferal oxygen isotopes. *Earth Sci. Rev.* **172**, 224–247 (2017).
38. T. Dunkley Jones *et al.*, OPTiMAL: A new machine learning approach for GDGT-based palaeothermometry. *Clim. Past* **16**, 2599–2617 (2020).
39. A. Pearson *et al.*, Factors controlling the distribution of archaeal tetraethers in terrestrial hot springs. *Appl. Environ. Microbiol.* **74**, 3523–3532 (2008).
40. A. Pitcher *et al.*, Crenarchaeol dominates the membrane lipids of *Candidatus* Nitrososphaera gargensis, a thermophilic group I.1b Archaeon. *ISME J.* **4**, 542–552 (2010).
41. F. J. Elling *et al.*, Chemotaxonomic characterisation of the thaumarchaeal lipidome. *Environ. Microbiol.* **19**, 2681–2700 (2017).
42. N. J. Bale *et al.*, Membrane lipid composition of the moderately thermophilic ammonia-oxidizing archaeon "*Candidatus* Nitrosotenuis uzonensis" at different growth temperatures. *Appl. Environ. Microbiol.* **85**, e01332-19 (2019).
43. A. Pitcher, S. Schouten, J. S. Sinninghe Damsté, In situ production of crenarchaeol in two California hot springs. *Appl. Environ. Microbiol.* **75**, 4443–4451 (2009).
44. C. L. Zhang, A. Pearson, Y. L. Li, G. Mills, J. Wiegel, Thermophilic temperature optimum for crenarchaeol synthesis and its implication for archaeal evolution. *Appl. Environ. Microbiol.* **72**, 4419–4422 (2006).
45. S. Schouten *et al.*, Archaeal and bacterial glycerol dialkyl glycerol tetraether lipids in hot springs of Yellowstone National Park. *Appl. Environ. Microbiol.* **73**, 6181–6191 (2007).
46. L. He, C. L. Zhang, H. Dong, B. Fang, G. Wang, Distribution of glycerol dialkyl glycerol tetraethers in Tibetan hot springs. *Geosci. Front.* **3**, 289–300 (2012).
47. E. Boyd, T. Hamilton, J. Wang, L. He, C. Zhang, The role of tetraether lipid composition in the adaptation of thermophilic Archaea to acidity. *Front. Microbiol.* **4**, 62 (2013).
48. W. Wu *et al.*, Impacts of temperature and pH on the distribution of archaeal lipids in Yunnan hot springs, China. *Front. Microbiol.* **4**, 312 (2013).
49. W. Xie *et al.*, Distribution of ether lipids and composition of the archaeal community in terrestrial geothermal springs: Impact of environmental variables. *Environ. Microbiol.* **17**, 1600–1614 (2015).
50. A. E. Ingalls *et al.*, Quantifying archaeal community autotrophy in the mesopelagic ocean using natural radiocarbon. *Proc. Natl. Acad. Sci. U.S.A.* **103**, 6442–6447 (2006).
51. C. Turich *et al.*, Lipids of marine Archaea: Patterns and provenance in the water-column and sediments. *Geochim. Cosmochim. Acta* **71**, 3272–3291 (2007).
52. K. W. R. Taylor, M. Huber, C. J. Hollis, M. T. Hernandez-Sanchez, R. D. Pancost, Re-evaluating modern and Palaeogene GDGT distributions: Implications for SST reconstructions. *Global Planet. Change* **108**, 158–174 (2013).
53. C. Zhu *et al.*, Stratification of archaeal membrane lipids in the ocean and implications for adaptation and chemotaxonomy of planktonic archaea. *Environ. Microbiol.* **18**, 4324–4336 (2016).
54. M. Sollai, L. Villanueva, E. C. Hopmans, R. G. Keil, J. S. Sinninghe Damsté, Archaeal sources of intact membrane lipid biomarkers in the oxygen deficient zone of the eastern tropical south pacific. *Front. Microbiol.* **10**, 765 (2019).
55. C. A. Francis, K. J. Roberts, J. M. Beman, A. E. Santoro, B. B. Oakley, Ubiquity and diversity of ammonia-oxidizing archaea in water columns and sediments of the ocean. *Proc. Natl. Acad. Sci. U.S.A.* **102**, 14683–14688 (2005).
56. S. J. Hallam *et al.*, Pathways of carbon assimilation and ammonia oxidation suggested by environmental genomic analyses of marine Crenarchaeota. *PLoS Biol.* **4**, e95 (2006).
57. A. E. Santoro, K. L. Casciotti, C. A. Francis, Activity, abundance and diversity of nitrifying archaea and bacteria in the central California Current. *Environ. Microbiol.* **12**, 1989–2006 (2010).
58. L. Villanueva, S. Schouten, J. S. Sinninghe Damsté, Depth-related distribution of a key gene of the tetraether lipid biosynthetic pathway in marine Thaumarchaeota. *Environ. Microbiol.* **17**, 3527–3539 (2015).
59. A. E. Santoro *et al.*, Genomic and proteomic characterization of "*Candidatus* Nitrosopelagicus brevis": An ammonia-oxidizing archaeon from the open ocean. *Proc. Natl. Acad. Sci. U.S.A.* **112**, 1173–1178 (2015).
60. R. J. E. Alves, B. Q. Minh, T. Urich, A. von Haeseler, C. Schleper, Unifying the global phylogeny and environmental distribution of ammonia-oxidising archaea based on *amoA* genes. *Nat. Commun.* **9**, 1517 (2018).
61. S. R. Shah, G. Mollenhauer, N. Ohkouchi, T. I. Eglinton, A. Pearson, Origins of archaeal tetraether lipids in sediments: Insights from radiocarbon analysis. *Geochim. Cosmochim. Acta* **72**, 4577–4594 (2008).
62. A. Pearson *et al.*, Stable carbon isotope ratios of intact GDGTs indicate heterogeneous sources to marine sediments. *Geochim. Cosmochim. Acta* **181**, 18–35 (2016).

63. J. H. Kim et al., New indices and calibrations derived from the distribution of crenarchaeal isoprenoid tetraether lipids: Implications for past sea surface temperature reconstructions. Geochim. Cosmochim. Acta 74, 4639–4654 (2010).

64. J. H. Kim et al., Influence of deep-water derived isoprenoid tetraether lipids on the TEX_{86}^H paleothermometer in the Mediterranean Sea. Geochim. Cosmochim. Acta 150, 125–141 (2015).

65. J. E. Tierney, M. P. Tingley, A TEX_{86} surface sediment database and extended Bayesian calibration. Sci. Data 2, 1–10 (2015).

66. A. Pan et al., A diagnostic GDGT signature for the impact of hydrothermal activity on surface deposits at the Southwest Indian Ridge. Org. Geochem. 99, 90–101 (2016).

67. S. J. Hurley, J. S. Lipp, H. G. Close, K. U. Hinrichs, A. Pearson, Distribution and export of isoprenoid tetraether lipids in suspended particulate matter from the water column of the Western Atlantic Ocean. Org. Geochem. 116, 90–102 (2018).

68. J. E. Tierney, J. S. Sinninghe Damsté, R. D. Pancost, A. Sluijs, J. C. Zachos, Eocene temperature gradients. Nat. Geosci. 10, 538–539 (2017).

69. Y. G. Zhang, X. Liu, Export depth of the TEX_{86} signal. Paleoceanogr. Paleoclimatol. 33, 666–671 (2018).

70. G. Trommer et al., Distribution of Crenarchaeota tetraether membrane lipids in surface sediments from the Red Sea. Org. Geochem. 40, 724–731 (2009).

71. I. Uda, A. Sugai, Y. H. Itoh, T. Itoh, Variation in molecular species of polar lipids from thermoplasma acidophilum depends on growth temperature. Lipids 36, 103–105 (2001).

72. I. Uda, A. Sugai, Y. H. Itoh, T. Itoh, Variation in molecular species of core lipids from the order thermoplasmales strains depends on the growth temperature. J. Oleo Sci. 53, 399–404 (2004).

73. Y. Wei et al., Spatial variations in archaeal lipids of surface water and core-top sediments in the South China Sea and their implications for paleoclimate studies. Appl. Environ. Microbiol. 77, 7479–7489 (2011).

74. G. Jia, X. Wang, W. Guo, L. Dong, Seasonal distribution of archaeal lipids in surface water and its constraint on their sources and the TEX_{86} temperature proxy in sediments of the South China Sea. J. Geophys. Res. 122, 592–606 (2017).

75. G. Jia, J. Zhang, J. Chen, P. Peng, C. L. Zhang, Archaeal tetraether lipids record subsurface water temperature in the South China Sea. Org. Geochem. 50, 68–77 (2012).

76. H. Dang et al., Thaumarchaeotal signature gene distribution in sediments of the northern South China Sea: An indicator of the metabolic intersection of the marine carbon, nitrogen, and phosphorus cycles? Appl. Environ. Microbiol. 79, 2137–2147 (2013).

77. D. Lai et al., Impact of terrestrial input on deep-sea benthic archaeal community structure in South China Sea sediments. Front. Microbiol. 11, 572017 (2020).

78. C. Zell et al., Sources and distributions of branched and isoprenoid tetraether lipids on the Amazon shelf and fan: Implications for the use of GDGT-based proxies in marine sediments. Geochim. Cosmochim. Acta 139, 293–312 (2014).

79. J. H. Kim, L. Villanueva, C. Zell, J. S. Sinninghe Damsté, Biological source and provenance of deep-water derived isoprenoid tetraether lipids along the Portuguese continental margin. Geochim. Cosmochim. Acta 172, 177–204 (2016).

80. E. C. Hopmans et al., A novel proxy for terrestrial organic matter in sediments based on branched and isoprenoid tetraether lipids. Earth Planet. Sci. Lett. 224, 107–116 (2004).

81. C. I. Blaga, G. J. Reichart, O. Heiri, J. S. Sinninghe Damsté, Tetraether membrane lipid distributions in water-column particulate matter and sediments: A study of 47 European lakes along a north–south transect. J. Paleolimnol. 41, 523–540 (2009).

82. J. S. Sinninghe Damsté, J. Ossebaar, S. Schouten, D. Verschuren, Distribution of tetraether lipids in the 25-ka sedimentary record of Lake Challa: Extracting reliable TEX_{86} and MBT/CBT palaeotemperatures from an equatorial African lake. Quat. Sci. Rev. 50, 43–54 (2012).

83. Y. G. Zhang et al., Methane index: A tetraether archaeal lipid biomarker indicator for detecting the instability of marine gas hydrates. Earth Planet. Sci. Lett. 307, 525–534 (2011).

84. C. R. Scotese, N. Wright, PALEOMAP paleodigital elevation models (PaleoDEMS) for the Phanerozoic (Tech. Rep., PALEOMAP Project, 2018).

85. J. H. Kim et al., An experimental field study to test the stability of lipids used for the TEX_{86} and $U_{37}^{K'}$ palaeothermometers. Geochim. Cosmochim. Acta 73, 2888–2898 (2009).

86. P. Y. Chenet, J. Francheteau, Bathymetric reconstruction method; application to the Central Atlantic Basin between 10°N and 40°N. Initial Rep. Deep Sea Drill. Proj. 51, 1501 (1980).

87. T. Westerhold et al., An astronomically dated record of Earth's climate and its predictability over the last 66 million years. Science 369, 1383–1387 (2020).

88. E. Grossman, M. Joachimski, –"Oxygen isotope stratigraphy" in Geologic Time Scale 2020, F. M. Gradstein, J. G. Ogg, M. D. Schmitz, G. M. Ogg, Eds. (Elsevier, 2020), chap. 10, pp. 279–307.

89. J. C. Zachos, G. R. Dickens, R. E. Zeebe, An early Cenozoic perspective on greenhouse warming and carbon-cycle dynamics. Nature 451, 279–283 (2008).

90. H. K. Coxall, P. A. Wilson, H. Pälike, C. H. Lear, J. Backman, Rapid stepwise onset of Antarctic glaciation and deeper calcite compensation in the Pacific Ocean. Nature 433, 53–57 (2005).

91. R. K. Via, D. J. Thomas, Evolution of Atlantic thermohaline circulation: Early Oligocene onset of deep-water production in the North Atlantic. Geology 34, 441–444 (2006).

92. M. E. Katz et al., Impact of Antarctic Circumpolar Current development on late Paleogene ocean structure. Science 332, 1076–1079 (2011).

93. A. Goldner, N. Herold, M. Huber, Antarctic glaciation caused ocean circulation changes at the Eocene-Oligocene transition. Nature 511, 574–577 (2014).

94. A. Olivarez Lyle, M. W. Lyle, Missing organic carbon in Eocene marine sediments: Is metabolism the biological feedback that maintains end-member climates? Paleoceanography 21, PA2007 (2006).

95. F. Boscolo-Galazzo et al., Temperature controls carbon cycling and biological evolution in the ocean twilight zone. Science 371, 1148–1152 (2021).

96. F. M. Gradstein, J. G. Ogg, M. D. Schmitz, G. M. Ogg, The Geologic Time Scale 2012 (Elsevier, 2012).

97. F. M. Gradstein, J. G. Ogg, M. D. Schmitz, G. M. Ogg, Geologic Time Scale 2020 (Elsevier, 2020).

98. G. Van Rossum, F. L. Drake, Python 3 Reference Manual (CreateSpace, 2009).

99. F. Pedregosa et al., Scikit-learn: Machine learning in Python. J. Mach. Learn. Res. 12, 2825–2830 (2011).

100. P. Virtanen et al.; SciPy 1.0 Contributors, SciPy 1.0: Fundamental algorithms for scientific computing in Python. Nat. Methods 17, 261–272 (2020).

101. S. Hoyer, J. Hamman, xarray: N-D labeled arrays and datasets in Python. J. Open Res. Softw. 5, 10 (2017).

102. M. Locarnini et al., Temperature, A. Mishonov, Ed. (World Ocean Atlas 2018, 2018), vol. 1.

103. M. Zweng et al., Salinity, A. Mishonov, Ed. (World Ocean Atlas 2018, 2019), vol. 2.

104. F. J. Millero, A. Poisson, International one-atmosphere equation of state of seawater. Deep Sea Res. A, Oceanogr. Res. Pap. 28, 625–629 (1981).

105. J. A. Boyden et al., Next-Generation Plate-Tectonic Reconstructions Using GPlates (Cambridge University Press, 2011).

106. H. D. Scher et al., Onset of Antarctic Circumpolar Current 30 million years ago as Tasmanian Gateway aligned with westerlies. Nature 523, 580–583 (2015).

107. C. M. Bishop, Pattern Recognition and Machine Learning (Information Science and Statistics, Springer, 2007).

108. R. De Maesschalck, D. Jouan-Rimbaud, D. L. Massart, The Mahalanobis distance. Chemom. Intell. Lab. Syst. 50, 1–18 (2000).

109. R. Rattanasriampaipong, Y. G. Zhang, A. Pearson, B. Hedlund, S. Zhang, Expanded compilations of isoprenoidal glycerol dialkyl glycerol tetraethers (GDGTs) in supplement to Rattanasriampaipong et al. "Archaeal lipids trace ecology and evolution of marine ammonia-oxidizing archaea" (2022). https://doi.org/10.6084/m9.figshare.20272866.v3 (Accessed 8 July 2022).

110. R. Rattanasriampaipong, Y. G. Zhang, A. Pearson, B. Hedlund, S. Zhang, Python scripts for statistical analysis and data visualization in supplement to Rattanasriampaipong et al. "Archaeal lipids trace ecology and evolution of marine ammonia-oxidizing archaea" (2022). https://doi.org/10.6084/m9.figshare.20272884.v4 (Accessed 8 July 2022).

111. M. T. Hernández-Sánchez, E. M. S. Woodward, K. W. R. Taylor, G. M. Henderson, R. D. Pancost, Variations in GDGT distributions through the water column of the South East Atlantic Ocean. Geochim. Cosmochim. Acta 132, 337–348 (2014).

112. S. L. Ho, M. Yamamoto, G. Mollenhauer, M. Minagawa, Core top TEX86 values in the south and equatorial Pacific. Org. Geochem. 42, 94–99 (2011).

113. S. L. Ho et al., Appraisal of TEX86 and TEX86L thermometries in subpolar and polar regions. Geochim. Cosmochim. Acta 131, 213–226 (2014).

114. A. Leider, K. U. Hinrichs, G. Mollenhauer, G. J. M. Versteegh, Core-top calibration of the lipid-based Uk'37 and TEX86 temperature proxies on the southern Italian shelf (SW Adriatic Sea, Gulf of Taranto). Earth Planet. Sci. Lett. 300, 112–124 (2010).

115. X. Lü et al., Sources and distribution of isoprenoid glycerol dialkyl glycerol tetraethers (GDGTs) in sediments from the east coastal sea of China: Application of GDGT-based paleothermometry to a shallow marginal sea. Org. Geochem. 75, 24–35 (2014).

116. A. Basse et al., Distribution intact core tetraether lipids water column profiles suspended particulate matter off Cape Blanc, NW Africa. Org. Geochem. 72, 1–13 (2014).

117. M. A. Besseling et al., Depth-related differences in archaeal populations impact the isoprenoid tetraether lipid composition of the Mediterranean Sea water column. Org. Geochem. 135, 16–31 (2019).

118. S. G. Wakeham, E. C. Hopmans, S. Schouten, J. S. Sinninghe Damsté, Archaeal lipids and anaerobic oxidation of methane in euxinic water columns: A comparative study of the Black Sea and Cariaco Basin. Chem. Geol. 205, 427–442 (2004).

119. S. Schouten et al., Intact polar and core glycerol dibiphytanyl glycerol tetraether lipids in the Arabian Sea oxygen minimum zone: I. Selective preservation and degradation in the water column and consequences for the TEX86. Geochim. Cosmochim. Acta 98, 228–243 (2012).

120. A. Auderset et al., Gulf Stream intensification after the early Pliocene shoaling of the Central American Seaway. Earth Planet. Sci. Lett. 520, 268–278 (2019).

121. P. K. Bijl et al., Maastrichtian-Rupelian paleoclimates in the southwest Pacific–A critical evaluation of biomarker paleothermometry and dinoflagellate cyst paleoecology at Ocean Drilling Program Site 1172. Clim. Past Discuss. 2021, 1–82 (2021).

122. M. J. Cramwinckel et al., Synchronous tropical and polar temperature evolution in the Eocene. Nature 559, 382–386 (2018).

123. D. De Vleeschouwer, B. F. Petrick, A. Martínez-García, Stepwise weakening of the Pliocene Leeuwin Current. Geophys. Res. Lett. 46, 8310–8319 (2019).

124. C. L. O'Brien et al., The enigma of Oligocene climate and global surface temperature evolution. Proc. Natl. Acad. Sci. U.S.A. 117, 25302–25309 (2020).

125. J. R. Super et al., North Atlantic temperature and pCO2 coupling in the early-middle Miocene. Geology 46, 519–522 (2018).

126. Y. G. Zhang, M. Pagani, Z. Liu, M. Bohaty Steven, R. DeConto, A 40-million-year history of atmospheric CO_2. Philos. Trans. R. Soc. A Math. Phys. Eng. Sci. 371, 20130096 (2013).

127. M. W. de Bar et al., Comparing seawater temperature proxy records for the past 90 Myrs from the shallow shelf record Bass River, New Jersey. Paleoceanogr. Paleoclimatol. 34, 455–475 (2019).

128. J. D. Hartman et al., Lipid biomarker results from the Oligocene and Miocene of IODP Hole 318-U1356 (2020). https://doi.pangaea.de/10.1594/PANGAEA.921643. Accessed 25 July 2022.

129. J. D. Hartman et al., Paleoceanography and ice sheet variability offshore Wilkes Land, Antarctica–Part 3: Insights from Oligocene-Miocene TEX86-based sea surface temperature reconstructions. Clim. Past 14, 1275–1297 (2018).

130. P. N. Pearson et al., Stable warm tropical climate through the Eocene Epoch. Geology 35, 211–214 (2007).

131. E. M. Crouch et al., Climatic and environmental changes across the early Eocene climatic optimum at mid-Waipara River, Canterbury Basin, New Zealand. Earth Sci. Rev. 200, 102961 (2020).

132. F. J. Elling et al., Archaeal lipid biomarker constraints on the Paleocene-Eocene carbon isotope excursion. Nat. Commun. 10, 4519 (2019).

133. F. Sangiorgi, W. Quaijtaal, T. H. Donders, S. Schouten, S. Louwye, Middle Miocene temperature and productivity evolution at a Northeast Atlantic Shelf Site (IODP U1318, Porcupine Basin): Global and regional changes. Paleoceanogr. Paleoclimatol. 36, e2020PA004059 (2021).

134. A. Sluijs et al., Late Paleocene-early Eocene Arctic Ocean sea surface temperatures: Reassessing biomarker paleothermometry at Lomonosov Ridge. Clim. Past 16, 2381–2400 (2020).

135. G. Zhuang, M. Pagani, Y. G. Zhang, Monsoonal upwelling in the western Arabian Sea since the middle Miocene. Geology 45, 655–658 (2017).

136. P. M. J. Douglas et al., Pronounced zonal heterogeneity in Eocene southern high-latitude sea surface temperatures. Proc. Natl. Acad. Sci. U.S.A. 111, 6582–6587 (2014).

137. C. Linnert et al., Evidence for global cooling in the Late Cretaceous. Nat. Commun. 5, 4194 (2014).

138. J. C. Zachos et al., Extreme warming of midlatitude coastal ocean during the Paleocene-Eocene Thermal Maximum: Inferences from TEX86 and isotope data. Geology 34, 737–740 (2006).

139. L. Cavalheiro et al., Impact of global cooling on Early Cretaceous high pCO2 world during the Weissert Event. Nat. Commun. 12, 5411 (2021).

140. L. K. O'Connor et al., Late Cretaceous temperature evolution of the southern high latitudes: A TEX86 perspective. *Paleoceanogr. Paleoclimatol.* **34**, 436–454 (2019).

141. S. A. Robinson et al., Southern Hemisphere sea-surface temperatures during the Cenomanian-Turonian: Implications for the termination of Oceanic Anoxic Event 2. *Geology* **47**, 131–134 (2019).

142. S. Steinig et al., Evidence for a regional warm bias in the Early Cretaceous TEX86 record. *Earth Planet. Sci. Lett.* **539**, 116184 (2020).

143. H. Alsenz et al., Sea surface temperature record of a Late Cretaceous tropical Southern Tethys upwelling system. *Paleogeogr. Paleoclimatol. Paleoecol.* **392**, 350–358 (2013).

144. A. Bornemann et al., Isotopic evidence for glaciation during the Cretaceous Supergreenhouse. *Science* **319**, 189–192 (2008).

145. C. Bottini et al., Climate variability and ocean fertility during the Aptian Stage. *Clim. Past* **11**, 383–402 (2015).

146. M. Dumitrescu, S. C. Brassell, S. Schouten, E. C. Hopmans, J. S. Sinninghe Damsté, Instability in tropical Pacific sea-surface temperatures during the early Aptian. *Geology* **34**, 833–836 (2006).

147. A. Forster, S. Schouten, M. Baas, J. S. Sinninghe Damsté, Mid-Cretaceous (Albian-Santonian) sea surface temperature record of the tropical Atlantic Ocean. *Geology* **35**, 919–922 (2007).

148. P. Hofmann, I. Stüsser, T. Wagner, S. Schouten, J. S. Sinninghe Damsté, Climate-ocean coupling off North-West Africa during the Lower Albian: The Oceanic Anoxic Event 1b. *Paleogeogr. Paleoclimatol. Paleoecol.* **262**, 157–165 (2008).

149. H. C. Jenkyns, L. Schouten-Huibers, S. Schouten, J. S. Sinninghe Damsté, Warm Middle Jurassic-Early Cretaceous high-latitude sea-surface temperatures from the Southern Ocean. *Clim. Past* **8**, 215–226 (2012).

150. K. Littler, S. A. Robinson, P. R. Bown, A. J. Nederbragt, R. D. Pancost, High sea-surface temperatures during the Early Cretaceous Epoch. *Nat. Geosci.* **4**, 169 (2011).

151. S. Schouten et al., Extremely high sea-surface temperatures at low latitudes during the middle Cretaceous as revealed by archaeal membrane lipids. *Geology* **31**, 1069–1072 (2003).

152. T. Wagner et al., Rapid warming and salinity changes of Cretaceous surface waters in the subtropical North Atlantic. *Geology* **36**, 203–206 (2008).

153. N. A. G. M. van Helmond et al., A perturbed hydrological cycle during Oceanic Anoxic Event 2. *Geology* **42**, 123–126 (2014).

154. N. A. G. M. van Helmond et al., Freshwater discharge controlled deposition of Cenomanian-Turonian black shales on the NW European epicontinental shelf (Wunstorf, northern Germany). *Clim. Past* **11**, 495–508 (2015).